



Cite this: *Phys. Chem. Chem. Phys.*,  
2021, 23, 22912

# Two-bond $^{13}\text{C}$ – $^{13}\text{C}$ spin-coupling constants in saccharides: dependencies on exocyclic hydroxyl group conformation†

Jieye Lin,<sup>a</sup> Reagan J. Meredith,<sup>a</sup> Allen G. Oliver,<sup>ib</sup> Ian Carmichael<sup>ib</sup> and Anthony S. Serianni<sup>ib</sup>\*<sup>a</sup>

Seven doubly  $^{13}\text{C}$ -labeled isotopomers of methyl  $\beta$ -D-glucopyranoside, methyl  $\beta$ -D-xylopyranoside, methyl  $\beta$ -D-galactopyranoside, methyl  $\beta$ -D-galactopyranosyl-(1 $\rightarrow$ 4)- $\beta$ -D-glucopyranoside and methyl  $\beta$ -D-galactopyranosyl-(1 $\rightarrow$ 4)- $\beta$ -D-xylopyranoside were prepared, crystallized, and studied by single-crystal X-ray crystallography and solid-state  $^{13}\text{C}$  NMR spectroscopy to determine experimentally the dependence of  $^2J_{\text{C}_1\text{C}_3}$  values in aldopyranosyl rings on the C1–C2–O2–H torsion angle,  $\theta_2$ , involving the C2 carbon of the C1–C2–C3 coupling pathway. Using X-ray crystal structures to determine  $\theta_2$  in crystalline samples and by selecting compounds that exhibit a relatively wide range of  $\theta_2$  values in the crystalline state,  $^2J_{\text{C}_1\text{C}_3}$  values measured in crystalline samples were plotted against  $\theta_2$  and the resulting plot compared to that obtained from density functional theory (DFT) calculations. For  $\theta_2$  values ranging from  $\sim 90^\circ$  to  $\sim 240^\circ$ , very good agreement was observed between the experimental and theoretical plots, providing strong validation of DFT-calculated spin-coupling dependencies on exocyclic C–O bond conformation involving the central carbon of geminal C–C–C coupling pathways. These findings provide new experimental evidence supporting the use of  $^2J_{\text{CCC}}$  values as non-conventional spin-coupling constraints in MA/AT conformational modeling of saccharides in solution, and the use of NMR spin-couplings not involving coupled hydroxyl hydrogens as indirect probes of C–O bond conformation. Solvomorphism was observed in crystalline  $\beta\text{Gal}$ -(1 $\rightarrow$ 4)- $\beta\text{GlcOCH}_3$  wherein the previously-reported methanol solvate form was found to spontaneously convert to a monohydrate upon air-drying, leading to small but discernible conformational changes in, and a new crystalline form of, this disaccharide.

Received 20th July 2021,  
Accepted 10th September 2021

DOI: 10.1039/d1cp03320d

rscl.li/pccp

## Introduction

Spin–spin coupling constants ( $J$ -couplings) measured by NMR spectroscopy have been used for decades to assign the structures

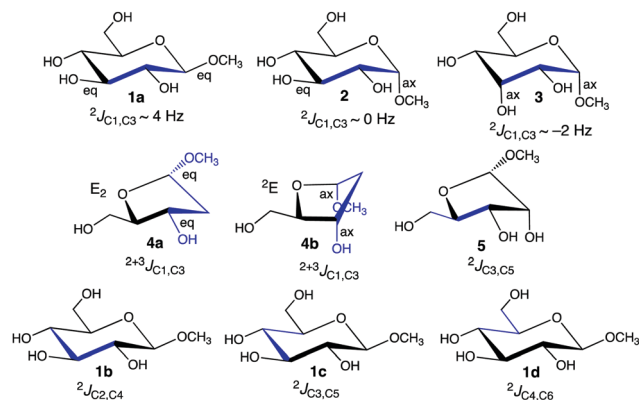
of molecules in solution.<sup>1–3</sup> Spin-couplings have been interpreted to infer bond lengths, valence bond angles, and dihedral angles, with the latter Karplus dependencies<sup>4</sup> of vicinal (three-bond)  $J$ -couplings such as  $^3J_{\text{HH}}$ ,  $^3J_{\text{CH}}$  and  $^3J_{\text{CC}}$  playing critical roles in determining conformational properties in solution.<sup>2,4–10</sup> Despite these advances, current practices are commonly limited to  $^3J$  values in structure determinations, most often  $^3J_{\text{HH}}$  values, and their interpretations are often qualitative or semi-quantitative. For example,  $^3J_{\text{HH}}$  values to model the conformational properties of exocyclic hydroxymethyl groups in saccharides make use of simplified three-state (staggered) models to interpret  $^3J_{\text{H}_5\text{H}_6\text{R}}$  and  $^3J_{\text{H}_5\text{H}_6\text{S}}$  values in aldohexopyranosyl rings.<sup>11,12</sup> In some cases, a limited group of  $^3J_{\text{HH}}$  values has been treated semi-quantitatively to infer the presence of predominant conformations in solution, the best known example being the PSEUROT method to investigate furanosyl ring conformational equilibria.<sup>13–15</sup> However, restricting such studies to  $^3J_{\text{HH}}$  values prevents unbiased modeling, especially in systems where two or more stable conformations

<sup>a</sup> Department of Chemistry and Biochemistry, University of Notre Dame, Notre Dame, IN 46556-5670, USA. E-mail: aserianni@nd.edu

<sup>b</sup> Molecular Structure Facility, University of Notre Dame, Notre Dame IN 46556-5670, USA

<sup>c</sup> The Radiation Laboratory, University of Notre Dame, Notre Dame, IN 46556-5670, USA

† Electronic supplementary information (ESI) available: Chemical synthesis, solution and solid-state NMR spectra, and X-ray crystallography of **6**<sup>1,3</sup>, **7**<sup>1,3</sup>, **8**<sup>1,3</sup>, **8**<sup>1,3</sup>, **9**<sup>1,3</sup> and **9**<sup>1,3</sup>; X-ray crystallography of **1**<sup>1,3</sup>; effect of solid-state NMR sample preparation on the crystal structure of **8**; fitting statistics from solid-state  $^{13}\text{C}$  NMR determinations of  $^2J_{\text{CCC}}$  values; plots of  $S/S_0$  vs.  $\tau$  to determine  $^2J_{\text{C}_1\text{C}_3}$  or  $^2J_{\text{C}_1'\text{C}_3'}$  in **6**<sup>1,3</sup>, **7**<sup>1,3</sup>, **8**<sup>1,3</sup>, **8**<sup>1,3</sup>, **9**<sup>1,3</sup> and **9**<sup>1,3</sup>; plot of eqn (6) used to determine  $\theta_2'$  for  $^2J_{\text{C}_1'\text{C}_3'}$  values of 6.3 and 6.5 Hz in **8**<sup>1,3</sup>; description of aqueous (1  $\mu\text{s}$ ) molecular dynamics simulations; discussion of eqn (1) for  $J$ -coupling equation parameterization; representative Cartesian coordinates for **1**<sup>c</sup>, **6**<sup>c</sup>, **7**<sup>c</sup>, **8**<sup>c</sup> and **9**<sup>c</sup>; complete ref. 28; ESI references. See DOI: 10.1039/d1cp03320d



**Scheme 1**  ${}^2J_{\text{CCC}}$  in different contexts in saccharides. Structures **1a-3**: configurational effects on  ${}^2J_{\text{C1,C3}}$ . Structures **4a/4b**: configurational effects on dual-pathway  ${}^{2+3}J_{\text{C1,C3}}$  in  $E_2$  and  ${}^2E$  furanose ring conformers. Structure **5**: single-pathway  ${}^2J_{\text{C3,C5}}$  in aldopentofuranosyl rings. Structures **1b-1d**:  ${}^2J_{\text{C2,C4}}$ ,  ${}^2J_{\text{C3,C5}}$  and  ${}^2J_{\text{C4,C6}}$ , respectively, in aldohexopyranosyl rings. Coupling pathways are highlighted in blue.

may coexist in equilibrium. Assumptions are commonly made about the conformational model in order to fit the available experimental data.

The recent development of MA'AT analysis<sup>16-19</sup> has shown that continuous and unbiased modeling comparable to that provided by MD simulation is possible provided that sufficient redundant  $J$ -couplings with desirable properties are available. Increasing the power and applicability of the MA'AT method requires that the structural dependencies of  $J$ -values in addition to  ${}^3J_{\text{HH}}$ , including  ${}^1J_{\text{CH}}$ ,  ${}^1J_{\text{CC}}$ ,  ${}^2J_{\text{CC}}$  and  ${}^2J_{\text{CH}}$ , be more completely understood. This study, which builds on prior work,<sup>20</sup> aimed to investigate the structural dependencies of  ${}^2J_{\text{CCC}}$  values in saccharides to establish their usefulness in MA'AT modeling.

${}^2J_{\text{CCC}}$  values are encountered in different contexts in saccharides (Scheme 1). Configurational effects are evident in aldohexopyranosyl rings **1a-3**, where relative configuration at the terminal coupled carbons affects the magnitude and sign of  ${}^2J_{\text{C1,C3}}$ .<sup>21-23</sup> This configurational effect also manifests itself in the coupling between C1 and C3 in aldofuranosyl rings, where ring conformation determines the relative orientations of oxygen substituents at C1 and C3, thus affecting the coupling (**4a/4b** in Scheme 1, and Fig. 1). In **4a/4b**, however, two pathways determine  ${}^{2+3}J_{\text{C1,C3}}$ , namely, C1-C2-C3, and C1-O4-C4-C3, and the observed coupling is believed to be the algebraic sum of both pathways.<sup>24,25</sup> By comparing only the  $E_2$  (**4a**)  ${}^2E$  (**4b**) conformers in which the torsion angle for the three-bond (vicinal) pathway is  $\sim 0^\circ$  (Scheme 1), the contribution from the two-bond pathway can be estimated. As expected, the  $E_2$  conformer having the C1-O1 and C3-O3 bonds in quasi-equatorial orientations produces a significantly more positive coupling than the  ${}^2E$  conformer in which both bonds are quasi-axial. These configurational effects can be investigated experimentally, especially in structures like **1-3**, and empirical rules developed to predict  ${}^2J_{\text{CCC}}$  in unknown structures.<sup>21,22</sup> However, superimposed on these configurational effects are conformational effects, namely, those involving rotations about the exocyclic C-O bonds

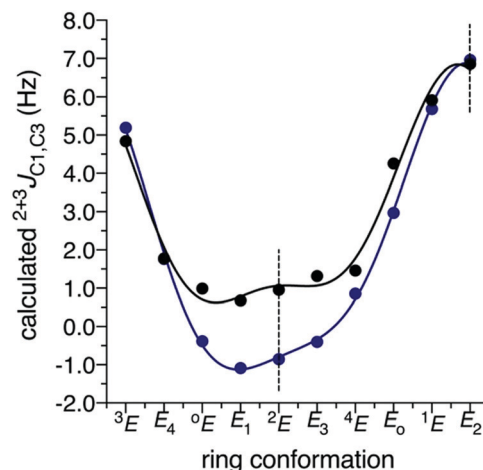


**Fig. 1** Effect of ring conformation on  ${}^{2+3}J_{\text{C1,C3}}$  in methyl  $\alpha$ -D-ribofuranoside (**5**) (black) and methyl 2-deoxy- $\alpha$ -D-erythro-pentofuranoside (methyl 2-deoxy- $\alpha$ -D-erythro-pentofuranoside) (**4a/4b**) (blue). Vertical dotted lines identify the north ( $E_2$ ) and south ( ${}^2E$ ) conformers that exhibit very different couplings due to the different relative orientations of the C1-O1 and C3-O3 bonds in the two conformers (Scheme 1). See text for discussion.

involving the three carbons in the C-C-C coupling pathway (Scheme 2). These effects can be significant,<sup>23</sup> as illustrated in Fig. 2. DFT calculations on **1** reveal that rotation about  $\theta_2$  exerts a much greater effect on  ${}^2J_{\text{C1,C3}}$  than rotations about  $\theta_1$  and  $\theta_3$  (Fig. 2). These effects predicted by DFT are difficult to validate experimentally, but the latter is essential for reliable and quantitative applications of  ${}^2J_{\text{CCC}}$  values in MA'AT analysis. This validation was pursued in this work by determining the effect of  $\theta_2$  on  ${}^2J_{\text{C1,C3}}$  in several  ${}^{13}\text{C}$ -labeled mono- and disaccharides (Scheme 3).

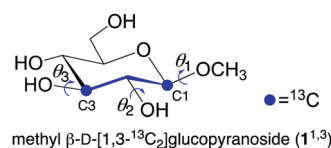
## Experimental

### A. Synthesis of $6^{1,3}$ , $7^{1,3}$ , $8^{1,3}$ , $8^{1,3'}$ , $9^{1,3}$ and $9^{1,3'}$

Synthetic procedures used to prepare doubly  ${}^{13}\text{C}$ -labeled mono-saccharides  $6^{1,3}$  and  $7^{1,3}$ , and disaccharides  $8^{1,3}$ ,  $8^{1,3'}$ ,  $9^{1,3}$  and  $9^{1,3'}$ , are available in the ESI.† Compound **1**<sup>1,3</sup> was prepared as described previously.<sup>20</sup>

### B. Measurements of ${}^{13}\text{C}$ - ${}^{13}\text{C}$ spin-couplings in solution and in crystalline $6^{1,3}$ , $7^{1,3}$ , $8^{1,3}$ , $8^{1,3'}$ , $9^{1,3}$ and $9^{1,3'}$

High-resolution 1D  ${}^{13}\text{C}\{^1\text{H}\}$  NMR spectra were obtained on  $6^{1,3}$ ,  $7^{1,3}$ ,  $8^{1,3}$ ,  $8^{1,3'}$ ,  $9^{1,3}$  and  $9^{1,3'}$  using 5 mm NMR tubes on a



**Scheme 2** Conformational determinants of  ${}^2J_{\text{C1,C3}}$  in **1**<sup>1,3</sup>. Coupling pathway is highlighted in blue. Rotation about  $\theta_2$  (C1-C2-O2-H torsion angle) is a major determinant of  ${}^2J_{\text{C1,C3}}$ . Rotations about  $\theta_1$  (C2-C1-O1-CH<sub>3</sub> torsion angle) and  $\theta_3$  (C2-C3-O3-H torsion angle) are minor determinants of  ${}^2J_{\text{C1,C3}}$ . Blue circles denote  ${}^{13}\text{C}$ -labeled carbons (99 atom%).

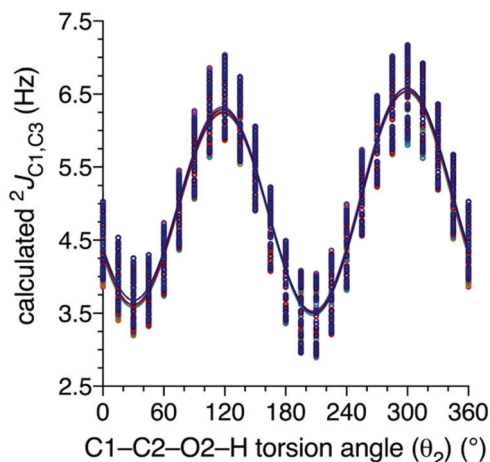


Fig. 2 Effects of  $\theta_1$ ,  $\theta_2$  and  $\theta_3$  on  ${}^2J_{C1,C3}$  in **1** calculated by DFT.  $\theta_2$  and  $\theta_3$  were each rotated through  $360^\circ$  in  $15^\circ$  increments while  $\theta_1$  was fixed at  $150^\circ$ ,  $165^\circ$ ,  $180^\circ$ ,  $195^\circ$ , and  $210^\circ$ . The plot shows the dependence of  ${}^2J_{C1,C3}$  on  $\theta_2$  where the overlapping solid lines are best fits to the five  $\theta_1$  datasets. Point scatter at discrete values of  $\theta_2$  shows the effects of  $\theta_1$  and  $\theta_3$  on  ${}^2J_{C1,C3}$ . The overall effect of  $\theta_2$  (dynamic range) is  $\sim 3.1$  Hz, whereas the averaged secondary effects of  $\theta_1$  and  $\theta_3$  are  $\sim \pm 0.6$  Hz. Adapted from Fig. 2.19 in ref. 23.

Varian DirectDrive 600 MHz FT-NMR spectrometer equipped with a 5 mm  ${}^1\text{H}$ - ${}^{19}\text{F}$ / ${}^{15}\text{N}$ - ${}^{31}\text{P}$  AutoX dual broadband probe. Spectra were collected in  ${}^2\text{H}_2\text{O}$  at  $22^\circ\text{C}$  with  $\sim 15\,000$  Hz spectral windows and  $\sim 4.5$  s recycle times, and were processed to give final digital resolutions of  $\sim 0.05$  Hz per pt.  ${}^{13}\text{C}$ - ${}^{13}\text{C}$  spin-couplings were obtained by analysis of the doublet character of the two intense signals arising from the mutually coupled  ${}^{13}\text{C}$ -labeled carbons in each compound (Fig. S1, S3, S5, S7, S9, and S11, ESI $^\dagger$ ). Since one of the  ${}^{13}\text{C}$ -labeled carbons in each of the six compounds is an anomeric carbon, non-first-order effects on the measurements of the  $J_{CC}$  values were negligible.

Crystalline samples of **6** $^{1,3}$ , **7** $^{1,3}$ , **8** $^{1,3}$ , **8** $^{1',3'}$ , **9** $^{1,3}$  and **9** $^{1',3'}$  ( $\sim 40$  mg of each) were mixed with KBr (60 : 40 w/w sample: KBr)

to give samples that contained an internal standard for *in situ* magic angle calibration.<sup>20</sup> All NMR measurements were performed on a JEOL ECX-300 solid-state FT-NMR spectrometer operating at a  ${}^1\text{H}$  frequency of 300 MHz and equipped with 3.2 mm magic angle spinning (MAS) probe. The magic angle ( $54.74^\circ$ ) was carefully adjusted on each sample by monitoring the  ${}^{79}\text{Br}$  signal arising from the internal KBr; spinning sidebands were observed to  $\sim 8$  ms. The MAS frequency was set to 16 kHz. At least three measurements of the  ${}^{13}\text{C}$ - ${}^{13}\text{C}$  spin-couplings were made on each sample.

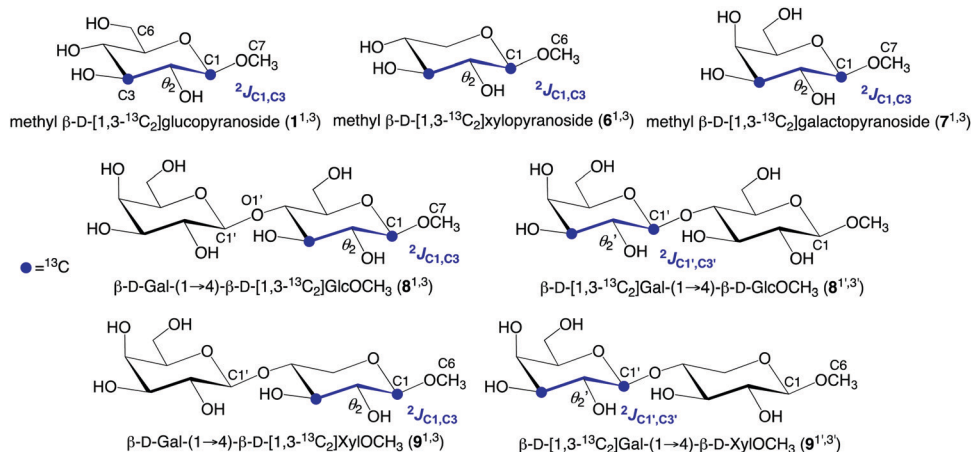
Cross-polarization magic-angle spinning 1D  ${}^{13}\text{C}$  NMR spectra of crystalline **6**–**9** contained signals arising from the  ${}^{13}\text{C}$ -labeled carbons only (Fig. S2, S4, S6, S8, S10 and S12, ESI $^\dagger$ ), giving spectra with sufficiently high signal-to-noise ratios to allow reliable determinations of signal integrations in  $J$ -modulated ( $S$ ) and reference ( $S_0$ ) spectra. The experimental  ${}^{13}\text{C}$ - ${}^{13}\text{C}$  spin-couplings were determined by fitting the plots of the  $S/S_0$  ratio as a function of  $\tau$  as described previously (Fig. S15, ESI $^\dagger$ ).<sup>20,26,27</sup> The reported  ${}^2J_{CC}$  values for each compound were obtained by averaging the  $J$ -couplings obtained from three sets of measurements on the sample, from which a standard deviation was computed.

The  ${}^2J_{C1,C3}$  values in **1** $^{1,3}$ , obtained from high-resolution  ${}^{13}\text{C}\{^1\text{H}\}$  and solid-state  ${}^{13}\text{C}$  NMR spectra, were taken from prior work.<sup>20</sup>

## Calculations

### A. Model structure **6** $^c$

**A.1. Geometry optimization.** Density functional theory (DFT) calculations were conducted in Gaussian16<sup>28</sup> using the B3LYP functional<sup>29</sup> and 6-311+g(d,p) basis set<sup>30,31</sup> for geometry optimization. In **6** $^c$  (the superscript “c” denotes an *in silico* structure), torsion angle  $\theta_1$  (C2–C1–O1–CH<sub>3</sub>) was fixed at the angle observed in crystalline **6** $^{1,3}$  ( $170.92^\circ$ ). Torsion angle  $\theta_2$  (C1–C2–O2–H) was set initially at  $180^\circ$  and rotated in  $15^\circ$  increments through  $360^\circ$  to give 24 optimized structures. The



Scheme 3 Chemical structures of seven selectively  ${}^{13}\text{C}$ -labeled mono- and disaccharides used in this study, and the  ${}^2J_{CC}$  value measured in each compound by solution- and solid-state  ${}^{13}\text{C}$  NMR. Blue circles, and the superscripts on compound numbers, denote the carbons labeled with  ${}^{13}\text{C}$  (99 atom%). The two-bond coupling pathways pertinent to each  ${}^2J_{CC}$  are highlighted in blue. Angle  $\theta_2$  corresponds to the C1–C2–O2–H torsion angle in **1** $^{1,3}$ , **6** $^{1,3}$ , **7** $^{1,3}$ , **8** $^{1,3}$  and **9** $^{1,3}$ , and angle  $\theta_2'$  to the C1'–C2'–C2'–H torsion angle in **8** $^{1',3'}$  and **9** $^{1',3'}$ .

remaining exocyclic torsion angles  $\theta_3$  and  $\theta_4$  (Scheme 3) were allowed to freely rotate during geometry optimization. The effect of solvent water was included in these calculations using the Self-Consistent Reaction Field (SCRF)<sup>32</sup> and the Integral Equation Formalism (polarizable continuum) model (IEFPCM)<sup>33</sup> as implemented in Gaussian16.

**A.2.  ${}^2J_{C1,C3}$  calculations in  $6^c$ .**  ${}^2J_{C1,C3}$  values were calculated in Gaussian16 as described previously.<sup>20</sup> The Fermi contact,<sup>34–36</sup> diamagnetic and paramagnetic spin-orbit, and spin-dipole<sup>34</sup> terms were calculated using the B3LYP functional and a tailored [5s2p1d|3s1p] basis set,<sup>12,37</sup> and the resulting  ${}^2J_{C1,C3}$  values were unscaled. All  $J$ -coupling calculations included the effect of solvent water, which was treated using the Self-Consistent Reaction Field (SCRF)<sup>32</sup> and the Integral Equation Formalism (polarizable continuum) model (IEFPCM)<sup>33</sup> as implemented in Gaussian16.

**A.3. Parameterization of  ${}^2J_{C1,C3}$  as a function of  $\theta_2$  in  $6^c$ .** The ensemble of geometry optimized structures of  $6^c$  and their associated calculated  ${}^2J_{C1,C3}$  values were inspected to remove low-probability, high-energy structures that might lead to aberrant equation parameterization. The remaining data were plotted as shown in Fig. 3, and the curve was fit to a modified Karplus-like equation (eqn (1)) using R (see ESI† for a brief discussion of eqn (1)). The goodness-of-fit of the equation is expressed as a root mean squared (RMSD) deviation.

$${}^2J_{C1,C3} \text{ (Hz)} = k + c1 \cos \theta_2 + s1 \sin \theta_2 + c2 \cos 2\theta_2 + s2 \sin 2\theta_2 + c3 \cos 3\theta_2 + s3 \sin 3\theta_2 \quad (1)$$

The parameterized equation relating  ${}^2J_{C1,C3}$  to  $\theta_2$  in  $6^c$  is shown as eqn (2).

$${}^2J_{C1,C3} \text{ (Hz)} = 5.08 - 0.12 \sin \theta_2 - 0.68 \cos 2\theta_2 - 1.27 \sin 2\theta_2 + 0.12 \sin 3\theta_2 \quad \text{RMSD} = 0.07 \text{ Hz} \quad (2)$$

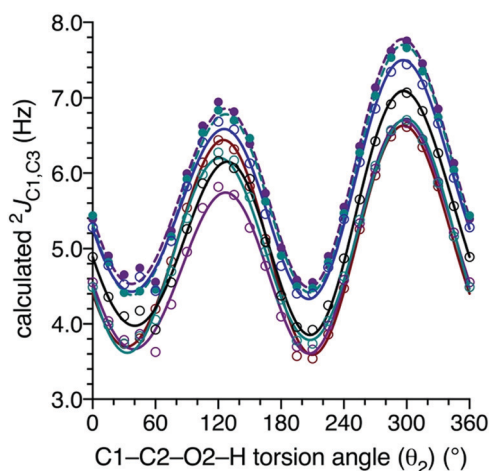


**Fig. 3** Plots of calculated  ${}^2J_{C1,C3}$  or  ${}^2J_{C1',C3'}$  in  $1^c$  and  $6^c$ – $9^c$  as a function of either  $\theta_2$  or  $\theta_2'$ . Solid and dashed lines correspond to the parameterized equations in the text. Open black/solid black line:  $1^c$ , eqn (3). Open blue/solid blue line:  $6^c$ , eqn (2). Open red/solid red line:  $7^c$ , eqn (4). Open green/solid green line:  $8^c$  ( ${}^2J_{C1,C3}$ ), eqn (5). Filled green; dashed green line:  $8^c$  ( ${}^2J_{C1',C3'}$ ), eqn (6). Open purple; solid purple line:  $9^c$  ( ${}^2J_{C1,C3}$ ), eqn (7). Filled purple/dashed purple line:  $9^c$  ( ${}^2J_{C1',C3'}$ ), eqn (8).

## B. Model structure $1^c$

DFT calculations on  $1^c$  were conducted as described for  $6^c$ . Torsion angle  $\theta_1$  (C2–C1–O1–CH<sub>3</sub>) was fixed at the angle observed in crystalline  $1^{1,3}$  (170.51°), and torsion angle  $\theta_2$  (C1–C2–O2–H) was rotated in 15° increments through 360°. The remaining exocyclic torsion angles ( $\theta_3$ – $\theta_6$ ; Scheme 4) were allowed to freely rotate during geometry optimization.  ${}^2J_{C1,C3}$  values were calculated in each conformer and plotted as a function of  $\theta_2$  (Fig. 3). The resulting curve was fit to give eqn (3).

$${}^2J_{C1,C3} \text{ (Hz)} = 5.27 + 0.19 \cos \theta_2 - 0.46 \sin \theta_2 - 0.57 \cos 2\theta_2 - 1.20 \sin 2\theta_2 + 0.16 \sin 3\theta_2 \quad \text{RMSD} = 0.11 \text{ Hz} \quad (3)$$

## C. Model structure $7^c$

DFT calculations on  $7^c$  were conducted as described for  $6^c$ . Torsion angle  $\theta_1$  (C2–C1–O1–CH<sub>3</sub>) was fixed at the angle observed in crystalline of  $7^{1,3}$  (163.41°) and torsion angle  $\theta_2$  (C1–C2–O2–H) was rotated through 360° in 15° increments. The remaining exocyclic torsion angles ( $\theta_3$ – $\theta_6$ ; Scheme 4) were allowed to freely rotate during geometry optimization.  ${}^2J_{C1,C3}$  values were calculated in each conformer and plotted as a function of  $\theta_2$  (Fig. 3). The resulting curve was fit to give eqn (4).

$${}^2J_{C1,C3} \text{ (Hz)} = 4.89 + 0.22 \cos \theta_2 - 0.88 \cos 2\theta_2 - 1.21 \sin 2\theta_2 \quad \text{RMSD} = 0.09 \text{ Hz} \quad (4)$$

## D. Model structure $8^c$ ( ${}^2J_{C1,C3}$ )

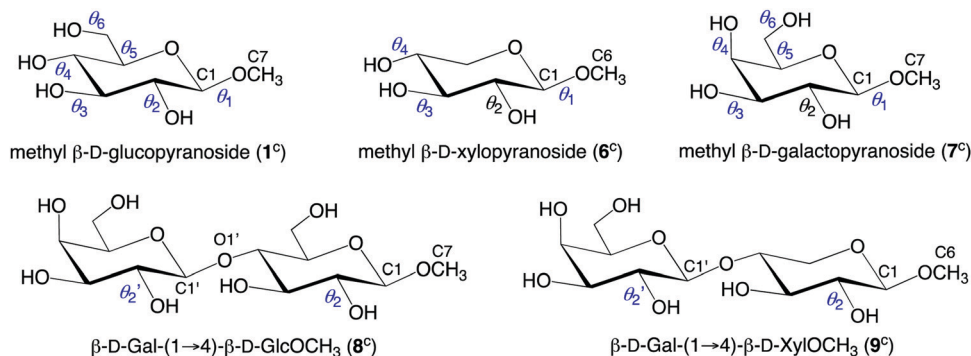
DFT calculations on  $8^c$  were conducted as described for  $6^c$ . The C2–C1–O1–CH<sub>3</sub> (164.14°), C2'–C1'–O1'–C4 (154.29°) and C1'–O1'–C4–C3 (78.28°) torsion angles were fixed at the respective angles observed in crystalline of  $8^{1,3}$ . Torsion angle  $\theta_2$  (C1–C2–O2–H) was rotated in 15° increments through 360°. The remaining exocyclic torsion angles were allowed to freely rotate during geometry optimization.  ${}^2J_{C1,C3}$  values were calculated in each conformer and plotted as a function of  $\theta_2$  (Fig. 3). The resulting curve was fit to give eqn (5).

$${}^2J_{C1,C3} \text{ (Hz)} = 5.09 - 0.27 \sin \theta_2 - 0.67 \cos 2\theta_2 - 1.20 \sin 2\theta_2 \quad \text{RMSD} = 0.10 \text{ Hz} \quad (5)$$

## E. Model structure $8^c$ ( ${}^2J_{C1',C3'}$ )

The C2–C1–O1–CH<sub>3</sub> (164.34°), C2'–C1'–O1'–C4 (153.98°) and C1'–O1'–C4–C3 (78.24°) torsion angles were fixed at the respective angles observed in crystalline  $8^{1,3}$ . Torsion angle  $\theta_2'$  (C1'–C2'–O2'–H) was rotated in 15° increments through 360°. The remaining exocyclic torsion angles were allowed to freely rotate during geometry optimization.  ${}^2J_{C1',C3'}$  values were calculated in each conformer and plotted as a function of  $\theta_2'$  (Fig. 3). The resulting curve was fit to give eqn (6).

$${}^2J_{C1',C3'} \text{ (Hz)} = 5.82 + 0.13 \cos \theta_2' - 0.47 \sin \theta_2' - 0.63 \cos 2\theta_2' - 1.25 \sin 2\theta_2' + 0.12 \sin 3\theta_2' \quad \text{RMSD} = 0.11 \text{ Hz} \quad (6)$$



**Scheme 4** Model structures **1<sup>c</sup>**, **6<sup>c</sup>**, **7<sup>c</sup>**, **8<sup>c</sup>** and **9<sup>c</sup>** used in DFT calculations of  ${}^2J_{C1,C3}$  or  ${}^2J_{C1',C3'}$  values, showing atom numbering and definitions of torsion angles  $\theta_1$ – $\theta_6$  in **1<sup>c</sup>**, **6<sup>c</sup>** and **7<sup>c</sup>**, and  $\theta_2$  and  $\theta_2'$  in **8<sup>c</sup>** and **9<sup>c</sup>**.

### F. Model structure **9<sup>c</sup>** ( ${}^2J_{C1,C3}$ )

DFT calculations on **9<sup>c</sup>** were conducted as described for **6<sup>c</sup>**. The C2–C1–O1–CH<sub>3</sub> (164.32°), C2'–C1'–O1'–C4 (156.49°) and C1'–O1'–C4–C3 (93.93°) torsion angles were fixed at the respective angles observed in crystalline **9<sup>1,3</sup>**.<sup>38</sup> Torsion angle  $\theta_2$  (C1–C2–O2–H) was rotated in 15° increments through 360°. The remaining exocyclic torsion angles were allowed to freely rotate during geometry optimization.  ${}^2J_{C1,C3}$  values were calculated in each conformer and plotted as a function of  $\theta_2$  (Fig. 3). The resulting curve was fit to give eqn (7).

$${}^2J_{C1,C3} \text{ (Hz)} = 4.93 + 0.19 \cos \theta_2 - 0.46 \sin \theta_2 - 0.57 \cos 2\theta_2 - 1.13 \sin 2\theta_2 + 0.12 \sin 3\theta_2 \quad \text{RMSD} = 0.10 \text{ Hz} \quad (7)$$

### G. Model structure **9<sup>c</sup>** ( ${}^2J_{C1',C3'}$ )

DFT calculations on **9<sup>c</sup>** were conducted as described for **6<sup>c</sup>**. The C2–C1–O1–CH<sub>3</sub> (164.32°), C2'–C1'–O1'–C4 (156.49°) and C1'–O1'–C4–C3 (93.93°) torsion angles were fixed at the respective angles observed in crystalline **9<sup>1,3</sup>**.<sup>38</sup> Torsion angle  $\theta_2'$  (C1'–C2'–O2'–H) was rotated in 15° increments through 360°. The remaining exocyclic torsion angles were allowed to freely rotate during geometry optimization.  ${}^2J_{C1',C3'}$  values were calculated in each conformer and plotted as a function of  $\theta_2'$  (Fig. 3). The resulting curve was fit to give eqn (8).

$${}^2J_{C1',C3'} \text{ (Hz)} = 5.91 + 0.15 \cos \theta_2' - 0.46 \sin \theta_2' - 0.65 \cos 2\theta_2' - 1.22 \sin 2\theta_2' + 0.14 \sin 3\theta_2' \quad \text{RMSD} = 0.11 \text{ Hz} \quad (8)$$

### H. Generalized equation relating ${}^2J_{C1,C3}$ / ${}^2J_{C1',C3'}$ to $\theta_2/\theta_2'$ in **1<sup>c</sup>** and **6<sup>c</sup>–9<sup>c</sup>**

Inspection of the plot in Fig. 3 shows the individual curves for **1<sup>c</sup>** and **6<sup>c</sup>–9<sup>c</sup>** (from eqn (2)–(8)) to be similar in shape but having y-axis displacements of up to ~1 Hz. This behavior allowed these curves to be averaged to give a generalized equation that relates  ${}^2J_{C1,C3}$ / ${}^2J_{C1',C3'}$  to  $\theta_2/\theta_2'$  in **1** and **6–9** (eqn (9)).

$${}^2J_{C1,C3} \text{ (general)} \text{ (Hz)} = 5.29 + 0.14 \cos \theta_2 - 0.33 \sin \theta_2 - 0.67 \cos 2\theta_2 - 1.21 \sin 2\theta_2 + 0.11 \sin 3\theta_2 \quad \text{RMSD} = 0.43 \text{ Hz} \quad (9)$$

### I. Aqueous molecular dynamics simulations of **1<sup>c</sup>**, **7<sup>c</sup>**, **8<sup>c</sup>** and **9<sup>c</sup>**

Aqueous (1 μs) molecular dynamics simulations were run on structures **1<sup>c</sup>**, **7<sup>c</sup>**, **8<sup>c</sup>** and **9<sup>c</sup>**. These calculations are described in the ESI.†

## Results and discussion

### A. C1–C2–C3 coupling pathway structure in, and NMR spectral properties of, compounds **1** and **6–9**

The configurations at C1, C2 and C3 in the C1–C2–C3 coupling pathways of monosaccharides **1**, **6** and **7** are identical, and these configurations in both residues of disaccharides **8** and **9** are identical to those found in **1**, **6** and **7**. This uniformity eliminates the effect of configuration at the terminal coupled C1 and C3 carbons, and the smaller effect of configuration at the intervening C2, thus allowing direct comparisons of experimental  ${}^2J_{C1,C3}$  and  ${}^2J_{C1',C3'}$  in seven different pathways.

This study sought validation of the effects of C2–O2 bond rotation on  ${}^2J_{C1,C3}$  as determined by DFT calculations (Fig. 2). Compounds **1** and **6–9** were selected because their crystal structures reveal C1–C2–O2–H ( $\theta_2$ ) or C1'–C2'–O2'–H ( $\theta_2'$ ) torsion angles ranging from 85.1° to 237.9° (Table 1 and Tables S1–S4, ESI†), covering ~40% of the available 360° range to interrogate the effect of  $\theta_2$  or  $\theta_2'$  on  ${}^2J_{C1,C3}$  sufficiently. Solid-state <sup>13</sup>C NMR spectra of **1<sup>1,3</sup>**, **6<sup>1,3</sup>**, **7<sup>1,3</sup>**, **8<sup>1,3</sup>**, **9<sup>1,3</sup>** and **9<sup>1',3'</sup>** contained two signals arising from the two <sup>13</sup>C-labeled carbons (Fig. S2, S4, S6, S10 and S12, ESI†), whereas that of **8<sup>1',3'</sup>** contained two pairs of signals indicating the presence of structural heterogeneity in the crystal (Fig. S8, ESI†). However, the high-resolution <sup>13</sup>C{<sup>1</sup>H} NMR spectrum of **8<sup>1',3'</sup>** indicated the presence of only one form in aqueous solution (Fig. S7, ESI†). This behavior was also observed in recent solid-state <sup>13</sup>C NMR studies of trans-*O*-glycosidic <sup>3</sup>J<sub>GOC</sub> values in **8**.<sup>20</sup> The cause of this structural heterogeneity in the crystalline state is attributed to replacement of lattice methanol with water during sample preparation for solid-state <sup>13</sup>C NMR measurements (sample drying prior to rotor packing) (see discussion below).

The C2–C1–O1–CH<sub>3</sub> and C2'–C1'–O1'–C4 torsion angles in **1<sup>1,3</sup>**, **6<sup>1,3</sup>**, **7<sup>1,3</sup>**, **8<sup>1,3</sup>**, **8<sup>1',3'</sup>**, **9<sup>1,3</sup>** and **9<sup>1',3'</sup>** sample limited ranges of 163–171° and 154–156°, respectively, as expected since both are

partly controlled by the *exo*-anomeric effect.<sup>40</sup> These relatively small changes in C1–O1 bond conformation exert only minor effects on  ${}^2J_{C1,C3}$  values (0.2 Hz or less). The C2–C3–O3–H ( $\theta_3$ ) and C2'–C3'–O3'–H ( $\theta_3'$ ) torsion angles range from 27–252°, and their influences on  ${}^2J_{C1,C3}$  and  ${}^2J_{C1',C3'}$  may be more substantial than that from C1–O1 bond rotation but are nevertheless likely to be small.<sup>20</sup> Relevant bond lengths and angles involving the C1–C3 and C1'–C3' carbons are also essentially constant and not expected to influence the magnitudes of  ${}^2J_{C1,C3}$  and  ${}^2J_{C1',C3'}$  appreciably.

### B. Calculated and experimental ${}^2J_{C1,C3}$ and ${}^2J_{C1',C3'}$ in crystalline samples and aqueous solutions of ${}^{13}\text{C}$ -labeled **1** and **6–9**

DFT-parameterized equations that relate  ${}^2J_{C1,C3}$  and  ${}^2J_{C1',C3'}$  to  $\theta_2$  or  $\theta_2'$ , respectively, in **1**<sup>c</sup> and **6**<sup>c</sup>–**9**<sup>c</sup> (eqn (2)–(8)) were used to calculate  ${}^2J_{\text{CCC}}$  values in crystalline **1**<sup>1,3</sup>, **6**<sup>1,3</sup>, **7**<sup>1,3</sup>, **8**<sup>1,3</sup>, **8**<sup>1',3'</sup>, **9**<sup>1,3</sup> and **9**<sup>1',3'</sup> based on the  $\theta_2$  or  $\theta_2'$  values observed in their crystal structures (Table 2).  ${}^2J_{C1,C3}$  and  ${}^2J_{C1',C3'}$  values were also calculated using generalized eqn (9) (Table 2). These calculated values were compared to  ${}^2J_{\text{CCC}}$  values obtained from solid-state  ${}^{13}\text{C}$  NMR measurements on the same samples used for crystallography, and to  ${}^2J_{\text{CCC}}$  values obtained from measurements on the same samples in aqueous solution (Table 2).

The information in Table 2 reveals that, in general,  ${}^2J_{C1,C3}$  values observed in aqueous solution are smaller than those observed in crystalline samples, with differences of up to 1.6 Hz ( ${}^2J_{C1',C3'}$  in **9**<sup>1',3'</sup>). An exception is the  $\beta\text{Glc}$  residue of **8** where  ${}^2J_{C1,C3}$  is larger in solution than in the crystalline state. Unlike the situation in crystalline samples, C2–O2 bond rotation is expected to be relatively free in aqueous solution, perhaps sampling all three staggered states, although the latter are probably not equally populated as suggested by MD simulation

(Fig. 4). General eqn (9) (Fig. 5) indicates that  ${}^2J_{C1,C3}$  is 4.4 Hz, 4.5 Hz and 7.0 Hz at  $\theta_2/\theta_2'$  values of 60°, 180° and 300°, respectively. If a three-state staggered model for rotation about the C2–O2 bond pertains, these observations suggest that the population of the 300° rotamer (H2 anti to OH2) is probably lower than those of the remaining two rotamers, given that the experimental  ${}^2J_{C1,C3}$  and  ${}^2J_{C1',C3'}$  values in aqueous solution assume values between 4–5 Hz (Table 2). In the crystalline state,  $\theta_2/\theta_2'$  adopts values that deviate significantly from staggered states, often leading to  ${}^2J_{C1,C3}$  and  ${}^2J_{C1',C3'}$  values that exceed those found in solution, especially since those associated with  $\theta_2/\theta_2' = 60^\circ$  and  $180^\circ$  lie at the lower end of the allowed range. The aberrant behavior of **8**<sup>1,3</sup> can be understood by noting that in the crystal,  $\theta_2 = 234^\circ$ , which yields an experimental  ${}^2J_{C1,C3}$  of 3.8 Hz, a value smaller than those observed in the three staggered C2–O2 rotamers.

Calculated and experimental values of  ${}^2J_{C1,C3}$  and  ${}^2J_{C1',C3'}$ , summarized in Table 2, are plotted as a function of  $\theta_2$  in Fig. 5, superimposed on the curve corresponding to eqn (9). In general, the experimental data fit the theoretical curve well, showing a maximal *J*-coupling of ~6.3 Hz at  $\theta_2 = 130^\circ$  and a minimal value of ~3.8 Hz at  $\theta_2 = 210^\circ$ . An inspection of Table 2 shows that five of the eight average calculated  ${}^2J_{\text{CCC}}$  values differ by <0.3 Hz from the experimental values, and two of the remaining three average calculated values are <0.8 Hz different from the experimental values. Considering the relatively modest dynamic range of the portion of the curve shown in Fig. 5 (~2.5 Hz) and the sources of error associated with equation parameterization and with the experimental measurements, the agreement between theory and experiment is very good with a RMSD of 0.61 Hz for the averaged calculated values. Within the region of the curve probed by the experimental measurements, the dependence of  ${}^2J_{C1,C3}$  on  $\theta_2$  predicted by DFT

Table 1 Structure parameters observed in low-temperature crystal structures of  ${}^{13}\text{C}$ -labeled **1** and **6–9**

Structure parameter <sup>a</sup>	Compound						
	<b>1</b> <sup>1,3</sup>	<b>6</b> <sup>1,3</sup>	<b>7</b> <sup>1,3</sup>	<b>8</b> <sup>1,3</sup>	<b>8</b> <sup>1',3'</sup>	<b>9</b> <sup>1,3</sup> / <b>9</b> <sup>1',3'</sup>	
CSD entry	MBDGP11 [ref. 39]	nd1909	nd1908	nd1917	nd1916	blactob	XAQLOS [ref. 38]
Torsion angle (°)							
C1–C2–O2–H ( $\theta_2$ )	91.5 (Glc)	85.1 (Xyl)	100.0 (Gal)	234.1 (Glc)	237.9 (Glc)	234.6 (Glc)	164.2 (Xyl)
C1'–C2'–O2'–H ( $\theta_2'$ )	—	—	—	154.8 (Gal)	146.7 (Gal)	153.6 (Gal)	113.0 (Gal)
C2–C1–O1–CH <sub>3</sub> ( $\phi$ )	170.6 (Glc)	170.9 (Xyl)	163.4 (Gal)	164.1 (Glc)	164.3 (Glc)	163.2 (Glc)	164.3 (Xyl)
C2'–C1'–O1'–C4 ( $\phi$ )	—	—	—	154.3 (Gal)	154.0 (Gal)	147.6 (Gal)	156.5 (Gal)
C1'–O1'–C4–C3 ( $\psi$ )	—	—	—	78.3	78.2	85.2	93.9
C2–C3–O3–H ( $\theta_3$ )	174.7 (Glc)	174.4 (Xyl)	27.1 (Gal)	198.9 (Glc)	203.8 (Glc)	193.3 (Glc)	198.9 (Xyl)
C2'–O3'–O3'–H ( $\theta_3'$ )	—	—	—	45.4 (Gal)	51.4 (Gal)	68.4 (Gal)	252.1 (Gal)
Bond angle (°)							
C1–C2–C3	108.0 (Glc)	107.8 (Xyl)	109.4 (Gal)	112.9 (Glc)	112.5 (Glc)	111.2 (Glc)	113.5 (Xyl)
C1'–C2'–C3'	—	—	—	108.4 (Gal)	108.2 (Gal)	108.6 (Gal)	108.2 (Gal)
Bond length (Å)							
C1–C2	1.525 (Glc)	1.528 (Xyl)	1.527 (Gal)	1.513 (Glc)	1.520 (Glc)	1.522 (Glc)	1.496 (Xyl)
C1'–C2'	—	—	—	1.524 (Gal)	1.530 (Gal)	1.524 (Gal)	1.530 (Gal)
C2–C3	1.521 (Glc)	1.524 (Xyl)	1.529 (Gal)	1.523 (Glc)	1.527 (Glc)	1.528 (Glc)	1.520 (Xyl)
C2'–C3'	—	—	—	1.530 (Gal)	1.533 (Gal)	1.528 (Gal)	1.529 (Gal)

<sup>a</sup> Errors in bond lengths ( $\pm 0.003$  Å), bond angles ( $\pm 0.2^\circ$ ), and torsion angles ( $\pm 0.2^\circ$ ) involving only heavy atoms were obtained from crystallographic analyses. Errors in torsion angles involving hydroxyl hydrogens ( $\pm 3^\circ$ ) were determined from a statistical analysis of X-ray structures obtained on thirteen different crystals of methyl  $\beta$ -lactoside (unpublished).

Table 2 Experimental and DFT-calculated  ${}^2J_{C1,C3}$  and  ${}^2J_{C1',C3'}$  Values in  ${}^{13}\text{C}$ -Labeled **1** and **6–9**

Compound	$\theta_2$ or $\theta_2'$ <sup>a</sup> (°)	${}^2J_{\text{CCC}}$	${}^2J_{\text{CCC}}$ (aqueous solution) <sup>b</sup> (Hz)	${}^2J_{\text{CCC}}$ (crystal) (Hz)	Calculated ${}^2J_{\text{CCC}}$ (eqn (2)–(8)) (Hz)	Calculated ${}^2J_{\text{CCC}}$ (eqn (9)) (Hz)	Average calculated ${}^2J_{\text{CCC}}$ <sup>c</sup> (Hz)	$\Delta^d$ (Hz)
<b>1</b> <sup>1,3</sup>	91.5 (Glc)	${}^2J_{C1,C3}$	4.6	5.2	5.3	5.6	5.5	−0.3
<b>6</b> <sup>1,3</sup>	85.1 (Xyl)	${}^2J_{C1,C3}$	4.2	5.2	5.3	5.3	5.3	−0.1
<b>7</b> <sup>1,3</sup>	100.0 (Gal)	${}^2J_{C1,C3}$	4.7	4.7	6.1	5.9	6.0	−1.3
<b>8</b> <sup>1,3</sup>	234.1 (Glc)	${}^2J_{C1,C3}$	4.6	3.8	4.4	4.5	4.4	−0.6
<b>8</b> <sup>1',3'</sup> (major)	146.7 (Gal)	${}^2J_{C1',C3'}$	5.1	6.5	6.5	5.9	6.2	0.3
<b>8</b> <sup>1',3'</sup> (minor)	153.6 (Gal)	${}^2J_{C1',C3'}$	5.1	6.3	6.2	5.7	6.0	0.3
<b>9</b> <sup>1,3</sup>	164.2 (Xyl)	${}^2J_{C1,C3}$	4.0	4.2	4.8	5.2	5.0	−0.8
<b>9</b> <sup>1',3'</sup>	113.0 (Gal)	${}^2J_{C1',C3'}$	4.9	6.5	6.7	6.2	6.5	0

<sup>a</sup> Errors in the C1–C2–O2–H and C1'–C2'–O2'–H torsion angles are  $\pm 3^\circ$  (see legend in Table 1). <sup>b</sup> Errors for the solution spin-couplings are  $\pm 0.1$  Hz; measured at 22 °C in  ${}^2\text{H}_2\text{O}$ . <sup>c</sup> Determined by averaging the values in both columns of calculated  ${}^2J_{\text{CCC}}$ . <sup>d</sup>  $\Delta = {}^2J_{\text{CCC}}$  (experimental) – average calculated  ${}^2J_{\text{CCC}}$ .

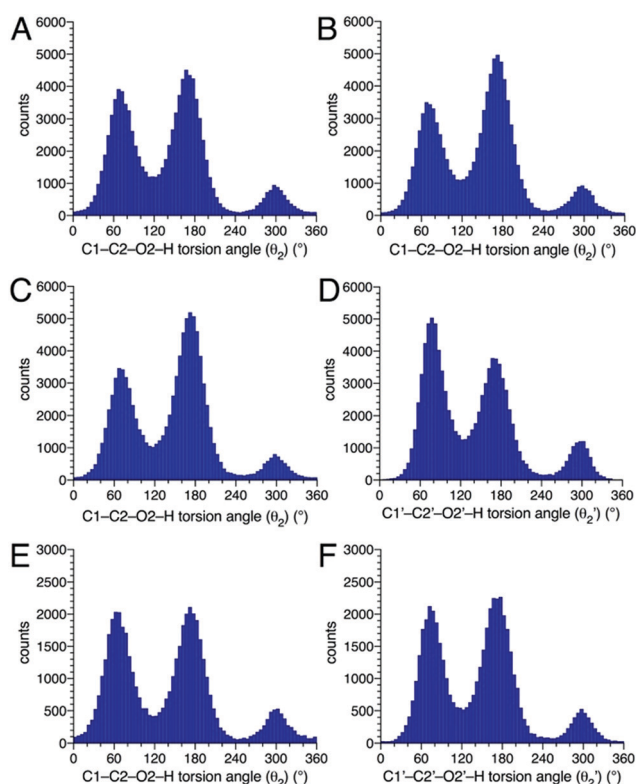


Fig. 4 Rotamer populations of the C2–O2 bond of **1** (A), **7** (B), **8** (C), and **9** (E), and the C2'–O2' bond in **8** (D) and **9** (F), determined by 1  $\mu\text{s}$  aqueous molecular dynamics simulations. In all cases, staggered rotamers dominate, with that having  $\theta_2$  or  $\theta_2'$  near  $300^\circ$  least preferred (see text).

is validated by the experimental measurements, confirming conclusions drawn earlier on a much more limited set of measurements.<sup>20</sup> It should be appreciated that the curve shown in Fig. 5 is a generalized curve obtained from averaging the structure-specific eqn (2)–(8), and that these equations, while describing similar curves, are nevertheless different, indicating that subtle undefined pathway differences in **2** and **6–9** affect the  ${}^2J_{\text{CCC}}$ . When the same data in Fig. 5 are superimposed on the ensemble of curves described by eqn (2)–(8) (Fig. 6), essentially all but one data point fall within the band of allowed  ${}^2J_{\text{CCC}}$  values produced by the ensemble of equations. The outlier is the

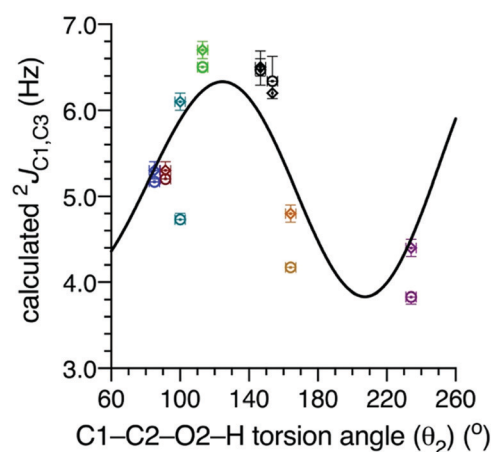


Fig. 5 Plot of eqn (9) (black line) superimposed on calculated and experimental  ${}^2J_{C1,C3}$  or  ${}^2J_{C1',C3'}$  values in **1** and **6–9**. Diamonds denote  ${}^2J_{\text{CCC}}$  values calculated by DFT. Circles denote experimental  ${}^2J_{\text{CCC}}$  values measured by solid-state  ${}^{13}\text{C}$  NMR. Red, **1**<sup>1,3</sup>. Blue, **6**<sup>1,3</sup>. Green, **7**<sup>1,3</sup>. Purple, **8**<sup>1,3</sup>. Black, **8**<sup>1',3'</sup> (major and minor). Orange, **9**<sup>1,3</sup>. Lime, **9**<sup>1',3'</sup>.

experimental  ${}^2J_{C1,C3}$  in methyl  $\beta$ -D-galactopyranoside **7** (Table 2), where the absolute difference between the average calculated  ${}^2J_{C1,C3}$  and the experimental  ${}^2J_{C1,C3}$  is 1.3 Hz. The origin of this discrepancy is unclear, but may result from (a) small cumulative effects of C3–O3, C4–O4 and/or C5–C6 conformation on equation parameterization, and (b) uncertainty in accurately locating the hydroxyl hydrogen at O2 in the X-ray crystal structure of **7** and consequently the C1–C2–O2–H torsion angle, since recent unpublished studies in this laboratory indicate uncertainties of up to  $\pm 3^\circ$  in C–C–O–H torsion angle determinations. The cumulative effect of several small errors caused by this simplification in the calculations could be partly responsible for the observed discrepancy. We cannot rule out, however, the possibility that the  ${}^2J_{C1,C3}$  vs.  $\theta_2$  curves calculated by DFT are phase-shifted to slightly higher values than found by experiment. Indeed, an inspection of Table 2 shows a general tendency for experimental  ${}^2J_{\text{CCC}}$  values to be smaller than calculated values. However, even if this is the case, the overall dependency of  ${}^2J_{C1,C3}$  on  $\theta_2$  observed in the experimental data replicates well that predicted by DFT in the region of  $\theta_2$  values interrogated by experiment.

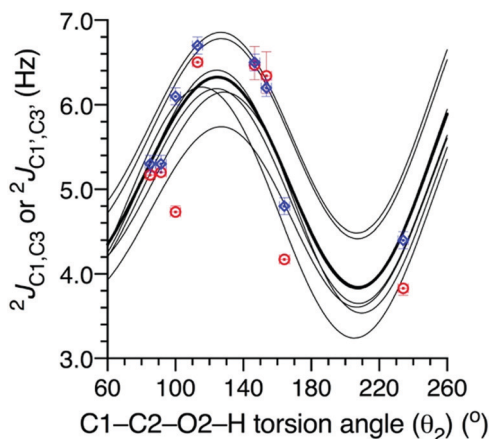


Fig. 6 Replot of the data in Fig. 5 showing that nearly all of the calculated (DFT) and experimental (solid-state  $^{13}\text{C}$  NMR)  ${}^2J_{\text{C1,C3}}$  values in **1** and **6–9** fall within the envelope defined by the seven curves describing eqn (2)–(8). The black curve in bold corresponds to eqn (9) (general equation). Blue diamonds denote  ${}^2J_{\text{CCC}}$  values calculated by DFT. Red circles denote experimental  ${}^2J_{\text{CCC}}$  values measured by solid-state  $^{13}\text{C}$  NMR.

### C. Origin of the pairs of signals in the solid-state $^{13}\text{C}$ NMR spectrum of $\mathbf{8}^{1',3'}$

Two pairs of  $^{13}\text{C}$  signals were observed in the solid-state  $^{13}\text{C}$  NMR spectrum of  $\mathbf{8}^{1',3'}$  (Fig. S8, ESI $^\dagger$ ). Similar behavior was observed previously in  $\mathbf{8}^{1',3}$ .<sup>20</sup> Dissolution of  $\mathbf{8}^{1',3'}$  (and  $\mathbf{8}^{1',3}$ ) in water and analysis of the resulting solutions by  $^{13}\text{C}\{^1\text{H}\}$  NMR revealed only one pair of signals arising from the two labeled carbons. These results suggest that two crystalline forms of **8** are possible. This behavior is caused by the loss of crystal-bound methanol during drying of the crystals and replacement by water (see “Effect of solid-state NMR sample preparation on the crystal structure of **8'** in ESI $^\dagger$ ). Drying crystals of **8** prior to packing the sample into solid-state NMR rotors results in crystal solvomorphism, one form being the methanol solvate and the other a monohydrate. Since the methanol oxygen serves as an hydrogen bond mono-acceptor with O4'H of the Gal residue, and as a donor with the more remote (relative to the C1–C2–C3 coupling pathway) O6 of the Glc residue, a change in solvation perturbs Gal residue  $^{13}\text{C}$  chemical shifts more than Glc  $^{13}\text{C}$  shifts, thus explaining why two pairs of signals are not observed in the solid-state  $^{13}\text{C}$  NMR spectrum of  $\mathbf{8}^{1',3}$ .

An alternate explanation was also entertained, namely, that the two pairs of signals arise from conformational differences mediated by solvent methanol–water exchange. The C1'–C2'–O2'–H torsion angle in crystals of  $\mathbf{8}^{1',3}$  (major) is  $146.7^\circ$ , while that in  $\mathbf{8}^{1',3'}$  (minor) is  $153.6^\circ$  (Table 1). This difference suggests that conformation about the C2'–O2' bond in **8** may be relatively mobile, varying over an  $10\text{--}15^\circ$  range in the lattice. Analysis of the solid-state  $^{13}\text{C}$  NMR spectrum of  $\mathbf{8}^{1',3'}$  gave  ${}^2J_{\text{C1',C3'}}$  values of 6.3 Hz (minor form) and 6.5 Hz (major form) (Table 2). Eqn (6) was used to determine  $\theta_2'$  values that correlate with these  $J$ -values (Fig. S15, ESI $^\dagger$ ). The 6.3 Hz value is consistent with  $\theta_2'$  values of  $101.4^\circ$ ,  $151.7^\circ$ ,  $255.9^\circ$  and  $340.4^\circ$ . The 6.5 Hz value is consistent with  $\theta_2'$  values of  $107.8^\circ$ ,  $145.7^\circ$ ,

$259.5^\circ$  and  $336.5^\circ$ . Experimental  $\theta_2'$  values of  $147^\circ$  and  $155^\circ$  are observed (Table 1), in good agreement with the  $146^\circ$  and  $152^\circ$  values calculated from eqn (6).

## Conclusions

The work described herein is part of a long-term research plan in this laboratory to develop a new NMR-based method to model the conformational properties of saccharides and other biomolecules in solution. Central to this plan is the development of MA'AT analysis<sup>16–19</sup> that utilizes experimental redundant NMR spin-coupling constants and DFT-parameterized spin-coupling equations to obtain continuous conformational models of *O*-glycoside linkages,<sup>16–18</sup> *O*-acetyl side-chains,<sup>19</sup> furanosyl rings and other conformational features of saccharides in solution. One benefit of this approach is that MA'AT models can be superimposed on those obtained by molecular dynamics simulation as a way to validate MD predictions, experimental validations that have been difficult to obtain previously.

The current study aimed to extend recent work<sup>20</sup> in which solid-state  $^{13}\text{C}$  NMR spectroscopy and single-crystal X-ray crystallography were used to investigate the conformational dependencies of  $^{13}\text{C}$ – $^{13}\text{C}$  spin-couplings in saccharides. Prior work has shown<sup>10,41</sup> that  ${}^3J_{\text{COCC}}$  and  ${}^3J_{\text{CCCC}}$  values in saccharides depend heavily on the C–O–C–C and C–C–C–C torsion angles, respectively, of the coupling pathways as expected based on analogy to the structural dependencies of other types of vicinal spin-couplings, notably  ${}^3J_{\text{HCCCH}}$ .<sup>1,2</sup> Less well understood are the conformational dependencies of  ${}^1J_{\text{CC}}$  and  ${}^2J_{\text{CC}}$  spin-couplings, the latter being the focus of attention in this work. Prior solution NMR studies had shown that intra-ring  ${}^2J_{\text{CCC}}$  values in aldopyranosyl rings depend strongly on the relative orientation of oxygen substituents appended to the terminal carbons of the C–C–C coupling pathway, with axial–axial, axial–equatorial and equatorial–equatorial arrangements giving very different magnitudes and signs of the coupling.<sup>21,22</sup> Superimposed on this configurational effect is the conformational dependence of  ${}^2J_{\text{CCC}}$  values wherein C–O bond rotation at any of the three carbons affects the  ${}^2J_{\text{CCC}}$ , with rotation about the C–O bond involving the central carbon showing the greater effect.<sup>23</sup> This property stimulated interest in the potential use of  ${}^2J_{\text{CCC}}$  values to investigate exocyclic C–O bond conformation in saccharides in solution by NMR without having to observe the hydroxyl hydrogen directly, the latter complicated by solvent exchange.<sup>42–45</sup>

The present work extends a recent study that applied the same experimental approach applied herein to  ${}^2J_{\text{CCC}}$  values in which a single exocyclic C–O torsion angle involving the central carbon was investigated.<sup>20</sup> While this prior study provided evidence that a combined solid-state  $^{13}\text{C}$  NMR and X-ray crystallography experimental strategy could be used to validate predicted behaviors determined by DFT calculations, the present work aimed to extend the experimental observations to an  $\sim 180^\circ$  range of C–O torsion angles to provide a more thorough test of the DFT calculations. The results demonstrate that the DFT method as implemented in this study gives very accurate



calculated  ${}^2J_{\text{CCC}}$  values and gives reliable and essentially quantitative predictions of their dependencies on exocyclic C–O torsion angles. This finding provides a strong incentive to use  ${}^2J_{\text{CCC}}$  values, when appropriate, as non-conventional spin-coupling constraints in MA'AT analyses of saccharides in future work.

Earlier studies revealed that the solid-state  ${}^{13}\text{C}$  NMR spectrum of methyl  $\beta$ -lactoside **8** labeled with  ${}^{13}\text{C}$  at C1 and C3 of the Gal residue contained two pairs of signals arising from the  ${}^{13}\text{C}$ -labeled carbons.<sup>20</sup> At the time, the origin of these paired signals was unclear, especially since the solution  ${}^{13}\text{C}\{^1\text{H}\}$  NMR spectrum of the same sample contained only one set of signals. This work has revealed that two stable forms of crystalline **8** are possible, one a methanol solvate and the other a monohydrate, with both solvent molecules occupying the same site. The methanol solvate, reported previously,<sup>46</sup> spontaneously converts to the monohydrate upon air-drying. The two crystals are not equivalent with respect to saccharide conformation, and are thus the likely cause of the paired solid-state  ${}^{13}\text{C}$  NMR signals observed previously. Inspection of the single-crystal X-ray structures of the methanol solvate and monohydrate forms of **8** reveals channels through which solvent molecules presumably travel to facilitate the solvomorphism. A driving force favoring the monohydrate may be attributed to its greater stability conferred by additional hydrogen bonding between the water and saccharide (*i.e.*, two hydrogen bonds in the methanol solvate *versus* three hydrogen bonds in the monohydrate), but other factors may affect this behavior. A more detailed treatment of the crystal structures of the two crystalline forms of **8** and a discussion of crystal lattice differences is forthcoming.

## Conflicts of interest

There are no conflicts of interest to declare.

## Acknowledgements

This work was supported by the National Science Foundation (CHE 1707660 and CHE 2002625 to A. S.) and by Omicron Biochemicals, Inc., South Bend, IN. The Notre Dame Radiation Laboratory is supported by the Department of Energy Office of Science, Office of Basic Energy Sciences, under Award Number DE-FC02-04ER15533. This is document number NDRL 5325.

## References

- C. A. G. Haasnoot, F. A. A. M. De Leeuw, H. P. M. De Leeuw and C. Altona, The relationship between proton–proton NMR coupling constants and substituent electronegativities. II—Conformational analysis of the sugar ring in nucleosides and nucleotides in solution using a generalized Karplus equation, *Org. Magn. Reson.*, 1981, **15**, 43–52.
- R. H. Contreras and J. E. Peralta, Angular dependence of spin-coupling constants, *Prog. NMR Spectrosc.*, 2000, **37**, 321–425.
- F. Li, J. H. Lee, A. Grishaev, J. Ying and A. Bax, High accuracy of Karplus equations for relating three-bond  $J$ -couplings to protein backbone torsion angles, *ChemPhysChem*, 2015, **16**, 572–578.
- M. Karplus, Contact electron-spin coupling of nuclear magnetic moments, *J. Chem. Phys.*, 1959, **30**, 11–15.
- R. U. Lemieux, R. K. Kullnig, H. J. Bernstein and W. G. Schneider, Configurational effects on the proton magnetic resonance spectra of six-membered ring compounds. 1, *J. Am. Chem. Soc.*, 1958, **80**, 6098–6105.
- M. Karplus, Vicinal proton coupling in nuclear magnetic resonance, *J. Am. Chem. Soc.*, 1963, **85**, 2870–2871.
- M. J. Minch, Orientational dependence of vicinal proton–proton NMR coupling constants: The Karplus relationship, *Concepts Magn. Reson.*, 1994, **6**, 41–56.
- B. Mulloy, T. Frenkiel and D. B. Davies, Long-range carbon–proton coupling constants: Application to conformational studies of oligosaccharides, *Carbohydr. Res.*, 1988, **184**, 39–46.
- I. Tvaroska and F. R. Taravel, Carbon–proton coupling constants in the conformational analysis of sugar molecules, *Adv. Carbohydr. Chem. Biochem.*, 1995, **51**, 15–61.
- B. Bose, S. Zhao, P. Bondo, G. Bondo, F. Cloran, I. Carmichael, R. Stenutz, B. Hertz and A. S. Serianni, Three-bond C–O–C–C spin-coupling constants in carbohydrates: Development of a Karplus relationship, *J. Am. Chem. Soc.*, 1998, **120**, 11158–11173.
- I. Tvaroska and J. Gajdos, Angular dependence of vicinal carbon–proton coupling constants for conformational studies of the hydroxymethyl group in carbohydrates, *Carbohydr. Res.*, 1995, **271**, 151–162.
- R. Stenutz, I. Carmichael, G. Widmalm and A. S. Serianni, Hydroxymethyl group conformation in saccharides: Structural dependencies of  ${}^2J_{\text{HH}}$ ,  ${}^3J_{\text{HH}}$ , and  ${}^1J_{\text{CH}}$  spin–spin coupling constants, *J. Org. Chem.*, 2002, **67**, 949–958.
- F. A. A. M. De Leeuw and C. Altona, Computer-assisted pseudorotation analysis of five-membered rings by means of proton–proton spin–spin coupling constants: Program PSEUROT, *J. Comput. Chem.*, 1983, **4**, 428–437.
- P. M. S. Hendrickx and J. C. Martins, A user-friendly Matlab program and GUI For the pseudorotation analysis of saturated five-membered ring systems based on scalar coupling constants, *Chem. Cent. J.*, 2008, **2**, 20–26.
- J. B. Houseknecht, C. Altona, C. M. Hadad and T. L. Lowary, Conformational analysis of furanose rings with PSEUROT: Parametrization for rings possessing the arabino, lyxo, ribo, and xylo stereochemistry and application to arabinofuranosides, *J. Org. Chem.*, 2002, **67**, 4647–4651.
- W. Zhang, T. Turney, R. Meredith, Q. Pan, L. Sernau, X. Wang, X. Hu, R. J. Woods, I. Carmichael and A. S. Serianni, Conformational populations of  $\beta$ -(1→4)  $O$ -glycosidic linkages using redundant NMR  $J$ -couplings and circular statistics, *J. Phys. Chem. B*, 2017, **121**, 3042–3058.
- W. Zhang, R. Meredith, M.-K. Yoon, X. Wang, R. J. Woods, I. Carmichael and A. S. Serianni, Synthesis and  $O$ -glycosidic linkage conformational analysis of  ${}^{13}\text{C}$ -labeled oligosaccharide fragments of an antifreeze glycolipid, *J. Org. Chem.*, 2019, **84**, 1706–1724.

- 18 W. Zhang, R. Meredith, Q. Pan, X. Wang, R. J. Woods, I. Carmichael and A. S. Serianni, Use of circular statistics to model  $\alpha$ Man-(1 $\rightarrow$ 2)- $\alpha$ Man and  $\alpha$ Man-(1 $\rightarrow$ 3)- $\alpha/\beta$ Man O-glycosidic linkage conformation in  $^{13}\text{C}$ -labeled disaccharides and high-mannose oligosaccharides, *Biochemistry*, 2019, **58**, 546–560.
- 19 T. Turney, Q. Pan, L. Sernau, I. Carmichael, W. Zhang, X. Wang, R. J. Woods and A. S. Serianni, O-Acetyl side-chains in monosaccharides: Redundant NMR spin-couplings and statistical models for acetate ester conformational analysis, *J. Phys. Chem. B*, 2017, **121**, 66–77.
- 20 W. Zhang, M.-K. Yoon, R. J. Meredith, J. Zajicek, A. G. Oliver, M. Hadad, M. H. Frey, I. Carmichael and A. S. Serianni,  $^{13}\text{C}$ - $^{13}\text{C}$  spin-coupling constants in crystalline  $^{13}\text{C}$ -labeled saccharides: Conformational effects interrogated by solid-state  $^{13}\text{C}$  NMR spectroscopy, *Phys. Chem. Chem. Phys.*, 2019, **21**, 23576–23588.
- 21 T. Church, I. Carmichael and A. S. Serianni, Two-bond  $^{13}\text{C}$ - $^{13}\text{C}$  spin-coupling constants in carbohydrates: Effect of structure on coupling magnitude and sign, *Carbohydr. Res.*, 1996, **280**, 177–186.
- 22 A. S. Serianni, P. B. Bondo and J. Zajicek, Verification of the projection resultant method for two-bond  $^{13}\text{C}$ - $^{13}\text{C}$  coupling sign determinations in carbohydrates, *J. Magn. Reson.*, 1996, **B112**, 69–74.
- 23 M. J. Hadad, W. Zhang, T. Turney, L. Sernau, X. Wang, R. J. Woods, A. Incandela, I. Surjancev, A. Wang, M.-K. Yoon, A. Coscia, C. Euell, R. Meredith, I. Carmichael and A. S. Serianni, in *NMR spin-couplings in saccharides: Relationships between structure, Conformation and the Magnitudes of  $J_{\text{HH}}$ ,  $J_{\text{CH}}$  and  $J_{\text{CC}}$  Values*, in *New Developments in NMR 10: NMR in Glycoscience and Glycotechnology*, ed. T. Peters and K. Kato, Royal Society of Chemistry, 2017, pp. 20–100.
- 24 J. L. Marshall, *Carbon–Carbon and Carbon–Proton NMR Couplings: Applications to Organic Stereochemistry and Conformational Analysis*, Verlag Chemie International, Deerfield Beach, FL, 1983, pp. 186–193.
- 25 T. J. Church, I. Carmichael and A. S. Serianni,  $^{13}\text{C}$ - $^1\text{H}$  and  $^{13}\text{C}$ - $^{13}\text{C}$  spin-coupling constants in methyl  $\beta$ -D-ribofuranoside and methyl 2-deoxy- $\beta$ -D-erythro-pentofuranoside: Correlations with molecular structure and conformation, *J. Am. Chem. Soc.*, 1997, **119**, 8946–8964.
- 26 P. Thureau, G. Mollica, F. Ziarelli and S. Viel, Selective measurements of long-range homonuclear  $J$ -couplings in solid-state NMR, *J. Mag. Reson.*, 2013, **231**, 90–94.
- 27 P. Thureau, I. Carvin, F. Ziarelli, S. Viel and G. Mollica, A Karplus equation for the conformational analysis of organic molecular crystals, *Angew. Chem.*, 2019, **131**, 16193–16197.
- 28 M. J. Frisch, *et al.*, *Gaussian 16, Revision B.01*, Gaussian Inc., Wallingford, CT, 2016, <https://gaussian.com/gaussian16/>.
- 29 A. D. Becke, Density-functional thermochemistry. III. The role of exact exchange, *J. Chem. Phys.*, 1993, **98**, 5648–5652.
- 30 A. D. McLean and G. S. Chandler, Contracted Gaussian basis sets for molecular calculations. I. Second row atoms,  $Z = 11$ –18, *J. Chem. Phys.*, 1980, **72**, 5639–5648.
- 31 R. B. J. S. Krishnan, J. S. Binkley, R. Seeger and J. A. Pople, Self-consistent molecular orbital methods. XX. A basis set for correlated wave functions, *J. Chem. Phys.*, 1980, **72**, 650–654.
- 32 E. Cancès, B. Mennucci and J. Tomasi, A new integral equation formalism for the polarizable continuum model: Theoretical background and applications to isotropic and anisotropic dielectrics, *J. Chem. Phys.*, 1997, **107**, 3032–3041.
- 33 R. Cammi, B. Mennucci and J. Tomasi, Fast evaluation of geometries and properties of excited molecules in solution: A Tamm–Dancoff model with application to 4-dimethylaminobenzonitrile, *J. Phys. Chem. A*, 2000, **104**, 5631–5637.
- 34 V. Sychrovský, J. Gräfenstein and D. Cremer, Nuclear magnetic resonance spin–spin coupling constants from coupled perturbed density functional theory, *J. Chem. Phys.*, 2000, **113**, 3530–3547.
- 35 T. Helgaker, M. Watson and N. C. Handy, Analytical calculation of nuclear magnetic resonance indirect spin–spin coupling constants at the generalized gradient approximation and hybrid levels of density-functional theory, *J. Chem. Phys.*, 2000, **113**, 9402–9409.
- 36 V. Barone, J. E. Peralta, R. H. Contreras and J. P. Snyder, DFT calculation of NMR  $J_{\text{FF}}$  spin–spin coupling constants in fluorinated pyridines, *J. Phys. Chem. A*, 2002, **106**, 5607–5612.
- 37 T. Klepach, H. Zhao, X. Hu, W. Zhang, R. Stenutz, M. J. Hadad, I. Carmichael and A. S. Serianni, Informing Saccharide Structural NMR Studies with Density Functional Theory Calculations, in *Glycoinformatics: Methods in Molecular Biology*, ed. T. Lütteke and M. Frank, Springer, New York, 2015, pp. 289–331.
- 38 W. Zhang, A. G. Oliver and A. S. Serianni, Disorder and conformational analysis of methyl  $\beta$ -D-galactopyranosyl-(1 $\rightarrow$ 4)- $\beta$ -D-xylopyranoside, *Acta Crystallogr., Sect. C: Cryst. Struct. Commun.*, 2012, **68**, o7–o11.
- 39 T. Turney, Q. Pan, W. Zhang, A. G. Oliver and A. S. Serianni, O-Benzoyl side-chain conformations in 2,3,4,6-tetra-O-benzoyl- $\beta$ -D-galactopyranosyl-(1 $\rightarrow$ 4)-1,2,6-tri-O-benzoyl- $\beta$ -D-glucopyranose (ethyl acetate solvate) and 1,2,4,6-tetra-O-benzoyl- $\beta$ -D-glucopyranose (acetone solvate), *Acta Crystallogr., Sect. C: Struct. Chem.*, 2019, **75**, 161–167.
- 40 E. Juaristi and G. Cuevas, *The Anomeric Effect*, CRC Press, Boca Raton, 1995, pp. 1–13, 95–109.
- 41 B. Bose, S. Zhao, P. Bondo, G. Bondo, F. Cloran, I. Carmichael, R. Stenutz, B. Hertz and A. S. Serianni, Three-bond C–O–C–C spin-coupling constants in carbohydrates: Development of a Karplus relationship, *J. Am. Chem. Soc.*, 1998, **120**, 11158–11173.
- 42 L. Kindahl, C. Sandström, T. Norberg and L. Kenne,  $^1\text{H}$  NMR studies of hydroxy protons of Asn- and Ser-linked disaccharides in aqueous solution, *J. Carbohydr. Chem.*, 2000, **19**, 1291–1303.
- 43 L. Poppe and H. van Halbeek, NMR spectroscopy of hydroxyl protons in supercooled carbohydrates, *Nat. Struct. Biol.*, 1994, **1**, 215–216.
- 44 B. Adams and L. Lerner, Observation of hydroxyl protons of sucrose in aqueous solution: No evidence for persistent intramolecular hydrogen bonds, *J. Am. Chem. Soc.*, 1992, **114**, 4827–4829.

- 45 H. Zhao, Q. Pan, W. Zhang, I. Carmichael and A. S. Serianni, DFT and NMR studies of  $^2J_{\text{COH}}$ ,  $^3J_{\text{HCOH}}$ , and  $^3J_{\text{CCOH}}$  spin-couplings in saccharides: C–O torsional bias and H-bonding in aqueous solution, *J. Org. Chem.*, 2007, **72**, 7071–7082.
- 46 R. Stenutz, M. Shang and A. S. Serianni, Methyl  $\beta$ -lactoside (methyl 4- $O$ - $\beta$ -D-galactopyranosyl- $\beta$ -D-glucopyranoside) methanol solvate, *Acta Crystallogr., Sect. C: Cryst. Struct. Commun.*, 1999, **55**, 1719–1721.